Reduced Cytotoxicity of Graphene Nanosheets Mediated by Blood-Protein Coating

Yu Chong,[†,⊥] Cuicui Ge,[†,⊥] Zaixing Yang,[†,⊥] Jose Antonio Garate,[‡] Zonglin Gu,[†] Jeffrey K. Weber,[‡] Jiajia Liu,[†] and Ruhong Zhou[*,†,‡,§]

[†]Institute of Quantitative Biology and Medicine, SRMP and RAD-X, Collaborative Innovation Center of Radiation Medicine of Jiangsu Higher Education Institutions, Soochow University, Suzhou 215123, China, [‡]IBM Thomas J. Watson Research Center, Yorktown Heights, New York 10598, United States, and [§]Department of Chemistry, Columbia University, New York, New York 10027, United States. [⊥]These authors contributed equally.

ABSTRACT The advent and pending wide use of nanoscale materials urges a biosafety assessment and safe design of nanomaterials that demonstrate applicability to human medicine. In biological microenvironment, biomolecules will bind onto nanoparticles forming corona and endow nanoparticles new biological identity. Since blood-circulatory system will most likely be the first interaction organ exposed to these nanomaterials, a deep understanding of the basic interaction mechanisms between serum proteins and foreign nanoparticles may help to better clarify the potential risks of nanomaterials and provide guidance on safe design of nanomaterials. In this study, the adsorption of four high-abundance blood proteins onto the carbon-based nanomaterial graphene oxide (GO) and reduced GO (rGO) were investigated *via* experimental (AFM, florescence spectroscopy, SPR) and simulation-based (molecular dynamics) approaches. Among the proteins in question, we observe competitive binding to the GO surface that features a mélange of distinct packing modes. Our MD simulations reveal that the protein adsorption is mainly enthalpically driven through strong $\pi-\pi$ stacking interactions between GO and aromatic protein residues, in addition to hydrophobic interactions. Overall, these results were in line with previous findings related to adsorption of serum proteins onto single-walled carbon nanotubes (SWCNTs), but GO exhibits a dramatic enhancement of adsorption capacity compared to this one-dimensional carbon form. Encouragingly, protein-coated GO resulted in a markedly less cytotoxicity than pristine and protein-coated SWCNTs, suggesting a useful role for this planar nanomaterial in biomedical applications.

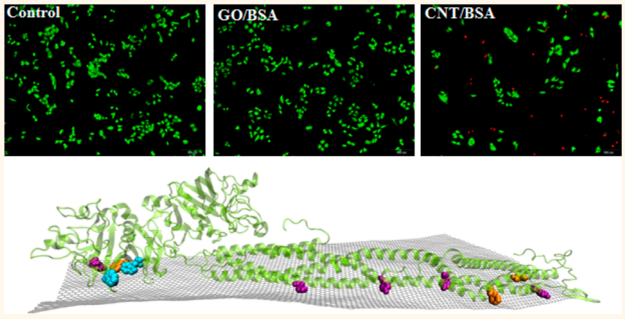

KEYWORDS: graphene · blood proteins · interactions · cytotoxicity · safe design

In recent years, manufactured nanomaterials have received increasing attention throughout a diverse range of biomedical fields. Promising applications of nanomaterials in areas such as cell imaging,[1] gene delivery,[2] and tumor therapy[3] foretell a preponderance of nanomaterial-based therapies in human medicine. Consequently, the emerging field of nanotoxicology (which focuses on elucidating the toxic effects of nanomaterials) is of paramount importance for the advancement of nanotherapeutics. Among nanomaterials that can be readily synthesized, materials in the graphite (sp^2) carbon family (*i.e.*, carbon nanotubes and graphene) have garnered particular interest due to their remarkable physical, morphological, and thermal and electrical conductivity properties.[3,4] Carbon nanotubes (CNTs), since their discovery,[5] have been utilized to great effect in biophysical applications like molecular detection,[6] and nanofluidic machines.[7] CNTs have shown promise in the context of nanomedicine: CNT-mediated targeted delivery of chemo- and photothera-peautic agents has been reported,[8−12] and optical imaging techniques that leverage functionalized CNTs have been employed in cellular detection applications.[12−14] Graphene, a two-dimensional analogue to CNTs, with its 2D structure, also presents unique physical and structural properties highlighting its use in areas such as electronics,[15,16] optics,[17,18] and biomedicine.[19,20] Among the latter, graphene has been proposed for application in *in vivo* photothermal ablation

* Address correspondence to ruhongz@us.ibm.com.

Received for review December 2, 2014 and accepted June 4, 2015.

Published online June 04, 2015
10.1021/nn5066606

© 2015 American Chemical Society

of tumors;[21] graphenes's high specific surface area renders it an ideal substrate for high-density biofunctionalization, facilitating the development of nanomaterial-based drug delivery systems. However, graphene is also implicated in foreign-body-induced carcinogenesis and tumor progression due to its active noncoated surface and long biopersistence.[22,23]

The broad application of CNTs and graphene to biomedicine is thus beset with a dichotomy of promising efficacy and secondary toxicity.[24−28] To develop safe nanomaterial-based biomedical applications, the nature of interactions between these nanostructured materials and tissues, cells, membranes, proteins, and generic biomolecules[29−31] must be well characterized. Following the above statement, CNTs have been shown to traverse cell membranes either *via* direct penetration[25,32] or endocytosis,[33,34] and CNT binding with pulmonary surfactant proteins has been correlated with susceptibility to lung infection and emphysema in mice.[35] In general, many studies have revealed that the effects of CNTs are related to interactions with a range of globular and intrinsically disordered proteins.[31,36,37] Meanwhile, graphene's interactions with cells and proteins are relatively less studied with more poorly understood. Recent studies have shown that graphene can directly interact with *Escherichia coli* membranes resulting in cytotoxic effect.[38−42] There have been a significant amount of toxicological studies on graphene and its derivatives, with emphasis on the interactions of nanoparticles with cells and proteins.[25,43−46] Many studies have shown that the presence of protein corona not only affects the uptake levels of nanoparticle by cells, but also results in remarkable differences in their biological effects.[47,48] The immobilization mechanisms of enzymes on graphene and GO were recently reviewed, as were the catalytic properties of the immobilized enzymes, and their applications.[49] It was also founded that HSA function was inhibited *via* blocking protein active sites or destroying protein structure.[50] In the same line, several studies have been performed about the effects of protein corona on the biological response of nanoparticles. For example, Dawson and co-workers found that adsorption of proteins on the nanoparticle surface strongly reduces its adhesion and causes a concomitant decrease in nanoparticle uptake efficiency.[51] Whether due to either environmental exposure or biomedical administration, it is very likely that the blood-circulatory system will be among the first organs to encounter carbon-based nanoparticles. In a recent study, GO coated with bovine serum albumin (BSA) greatly attenuated its toxicity;[43] however, there is still no study on the interaction of GO with these major and important blood proteins at atomic detail (and in particular, a detailed comparison among these blood proteins). Thus, there is a great need to systematically study the detailed interactions between GO and those important blood proteins, and to further reveal the molecular linkage between the protein adsorption and the cytotoxicity of GO. Four most abundant proteins including BSA, BFG, Ig, and Tf are chosen. Upon entering into the circulatory system, the surfaces of nanoparticles immediately adsorb these serum proteins, forming the so-called "nanoparticle-protein corona", which are the actual "entities" that the other cells encounter. The interaction of any nanoparticle with these coating proteins influences the cellular recognition and uptake of the nanoparticle, which eventually changes the biological response toward these foreign entities. Therefore, it is crucial to unveil the underlying interaction mechanism of nanoparticle with these proteins, as it helps to clarify the biological mechanism which can undoubtedly help toward the design of safer nanoparticle-based therapeutics, preventing/reducing any adverse effects of the aforementioned nanoparticles.

In previous work, we characterized the interactions between single walled carbon nanotubes (SWCNTs) and serum proteins using experiments and molecular dynamics simulations.[52] We observed competitive binding of proteins onto the SWCNT surface, with binding equilibrium and concomitant cytotoxicity moderated by protein structure and the hydrophobic amino acid content. In this study, we expand upon the interactions of serum proteins with graphene oxide nanosheets. Both experimental (fluorescence, circular dichroism, atomic force microscopy, surface plasmon resonance) and simulation-based (molecular dynamics) approaches are employed in order to fully characterize protein-coated graphene complexes, and cellular biological responses exposed to such complexes are evaluated *via* cytotoxicity assays. Overall, our results are well in line with our previous findings.[52] However, the protein absorption capacity of graphene is found to be much higher than that of SWCNTs, and more importantly, cytotocixity was dramatically reduced for the protein-coated graphene complexes.

RESULTS AND DISCUSSION

Adsorption Capacity and Kinetics. The adsorption capacities of four highly abundant blood proteins (bovine fibrinogen, BFG; immunoglobulin, Ig; transferrin, Tf; and bovine serum albumin, BSA) onto GO, reduced GO (rGO), and SWCNTs are shown in Figure 1 A, B, and C, respectively. On all cases, the nanomaterials present a consistent ordering of adsorption capacities for the studied proteins, that is BFG > Ig > Tf > BSA. At low mass ratio of protein to GO, the serum proteins are almost totally adsorbed. As the proportion for protein molecules is systematically increased, BFG maintains a near maximal extent of adsorption; Ig, Tf, and BSA fall off the full adsorption plateau at, respectively, lower protein concentrations (Figure 1A). This trend in adsorption capacity is mirrored by rGO and SWCNTs,

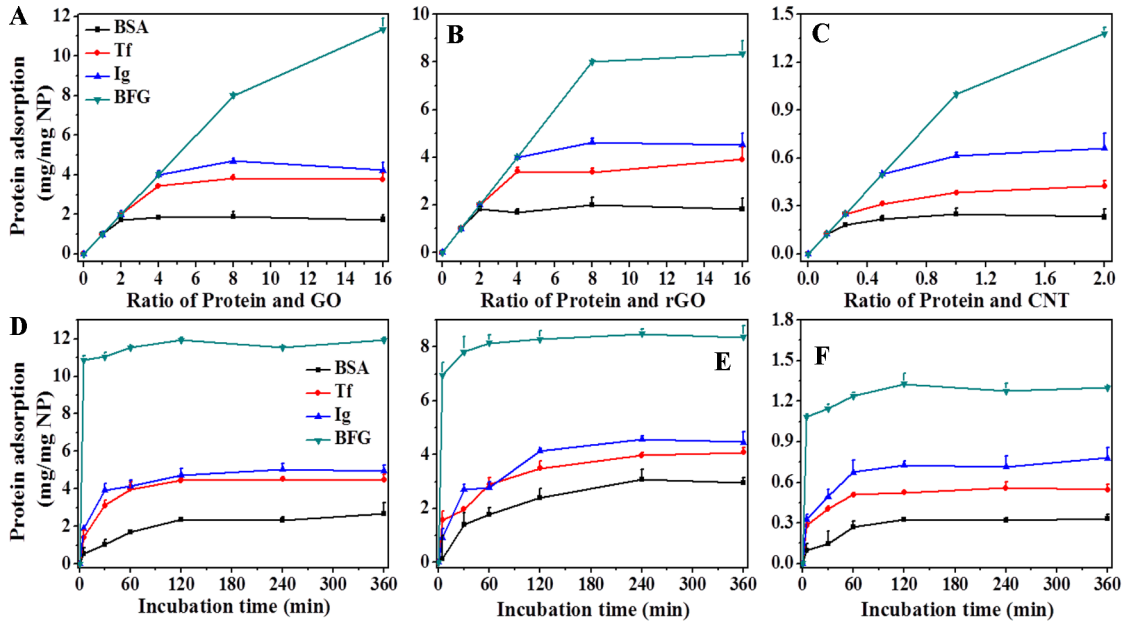

Figure 1. Quantitative analysis of serum protein adsorption onto various nanoparticles. The protein adsorption capacity was measured by the mass of protein adsorbed *vs* the mass ratio of protein to material through systematically increasing the ratio of protein to GO (A), rGO (B), and SWCNTs (C). The adsorption kinetics of protein bound to GO (D), rGO (E), and SWCNTs (F) were monitored at different incubation time points up to saturating concentrations of nanoparticles.

which also present accessible conjugated and hydrophobic surfaces to the protein substrates. However, there was a significant difference of protein adsorption capacity between GO sheets and SWCNT. Quantitatively, the adsorption capacities of GO and rGO are much higher than those of SWCNTs (Figure 1A–C). For example, the saturation adsorption content of BSA onto GO nanosheets was 2:1 (BSA to GO), compared with only 1:4 (BSA to SWCNT) for SWCNT, which implied protein adsorption capacity of GO nanosheets was eight times more than that of SWCNT. The four serum proteins studied exhibit similar results. Considering the difference in oxygen content between GO nanosheets and SWCNTs, the rGO (which features an oxygen content of only about 3%, making it difficult to disperse in water) might be more directly comparable to SWCNTs in terms of relative adsorption capacities. Although adsorption onto rGO (Figure 1B) was somewhat diminished when juxtaposed with the pure GO data, rGO adsorption still saturates much more slowly than in the SWCNT case. Perhaps unsurprisingly, thus, we find that adsorption onto graphene nanosheets with flat, exposed surfaces outstrips protein complex formation on highly curved nanotubes. Adsorption of a fifth protein (fetal bovine serum, FBS) onto the three classes of nanomaterial also confirms this prescribed trend in substrate topology (see Supporting Information Figure S1).

Adsorption kinetics is of great importance, as it allows to draw a dynamical picture of the protein–nanomaterial absorption phenomenon. By monitoring the fluorescence intensity of supernatant protein as a function of time, we found that the nanoparticle–protein binding process reached equilibrium within 60–120 min (Figure 1 D,E), with the planar substrates adsorbing much more protein in the first 5 min of interaction than their SWCNT counterparts. SDS–PAGE data confirm that GO nanosheets possess a higher adsorption capacity for highly abundant blood proteins than SWCNTs (Supporting Information Figure S2).

Binding Affinities. To better understand the interactions between GO sheets and serum proteins, binding affinities were measured using an Octet RED96 surface plasmon resonance system. Briefly, GO sheets were adsorbed onto streptavidin (SA) capture sensors to saturation. Subsequently, GO coated SA sensors were incubated with blood proteins over a concentration gradient to measure corresponding association and dissociation signals (Figure 2A–D). Different concentrations for the serum proteins were chosen because there was no valid response at concentration of BSA lower than 1 μM, and a concentration of IgG above 4 μM resulted in a signal beyond the limit. The resultant binding constant values (listed in Figure 2E) are ranked as follows: K_d (BFG) > K_d (Ig) > K_d (Tf) > K_d (BSA), consistent with the relative adsorption capacity trend observed above.

Adsorption Models and Adsorbed Protein Conformations. Atomic force microscopy (AFM) has been a useful tool in studying the distribution and morphology of protein. Here, we use AFM to study the adsorption model of GO sheets placed in contact with serum protein solutions. As demonstrated by Figure 3 and Supporting Information Figure S3, the four proteins exhibited different adsorption models on the surfaces of GO sheets in a manner consistent with data collected for

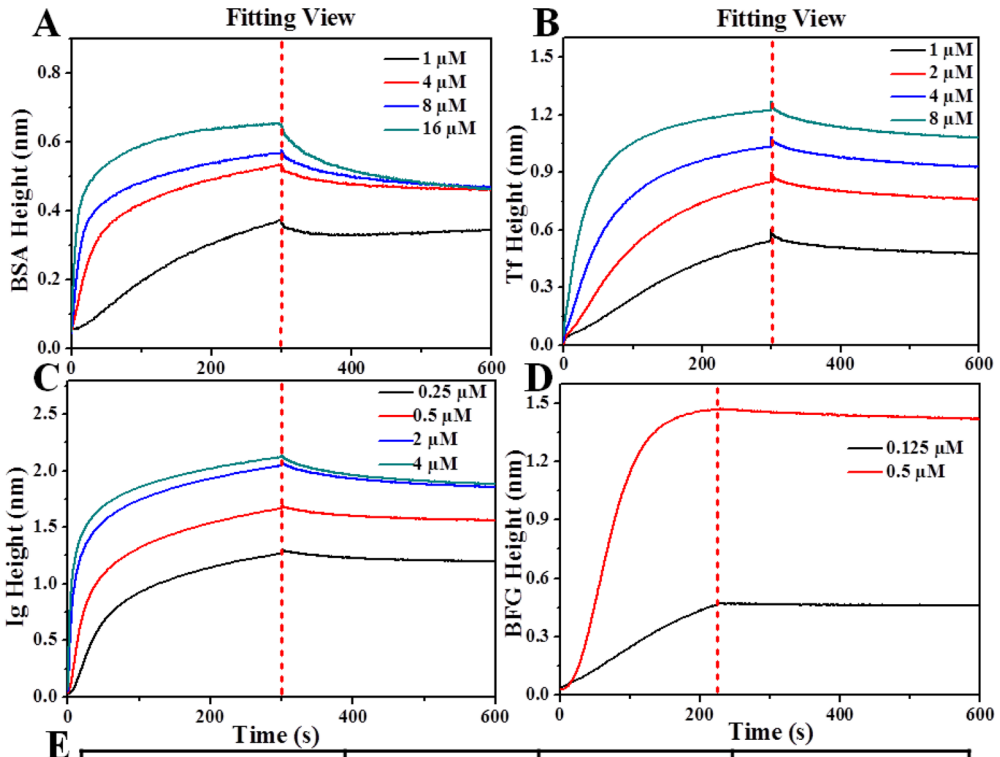

E

Sensor Type	Loading Sample	Sample ID	KD (M)
SA (Streptavidin)	GO	BSA	6.41×10^{-6}
SA (Streptavidin)	GO	Tf	3.66×10^{-6}
SA (Streptavidin)	GO	Ig	7.67×10^{-7}
SA (Streptavidin)	GO	BFG	1.97×10^{-7}

Figure 2. Measurements of protein–nanomaterial binding affinity. Association and dissociation curves of the four highly abundant blood proteins, interactions with GO sheets, are presented at top: BSA (A), Tf (B), IgG (C), BFG (D). Affinities for the GO–protein interactions were determined from these curves (E).

SWCNTs.[52] Upon first interaction, BSA appears to form complex aggregates that are spread uniformly over the GO surface; such aggregates change little over the course of incubation. This phenomenon was well confirmed by CD spectra. After just 5 min of incubation, BSA's CD spectrum was dramatically changed, with reduced α-helical features and enhanced β-sheet characteristics (Figure 3C), supporting the notion that β-rich aggregates form on the graphene surface. At 60 min of incubation time, no meaningful change was observed which implied that protein adsorption reached thermodynamic equilibrium. Tf exhibits a similar adsorption model to that seen for BSA, and CD measurements again confirm a complementary enhancement to β-sheet structure in adsorbed aggregates. Ig and BFG molecules were also found to adsorb onto GO surfaces with uniformity during the initial interaction process but, by contrast, tend toward a heterogeneous adsorption model as time continues. In support of this observation, CD spectra corresponding to BFG and Ig change drastically from 5 to 60 min, and the complex fine structure retained in each trace is suggestive of structural heterogeneity on the graphene surface. Differences between the uniform and heterogeneous modes of adsorption seen among these four proteins might be attributed to the prevalence of surface-exposed residues and differences among native protein structures; it should be noted, however, that all the observed adsorption processes were accompanied by substantial changes in protein secondary structure.

Molecular Dynamics Simulations of Protein Adsorption by Graphene. MD simulations, widely used in both biomolecular and nanomaterial simulations,[53,54] can provide a clear picture of the underlying molecular mechanisms which serve to drive the serum protein adsorption

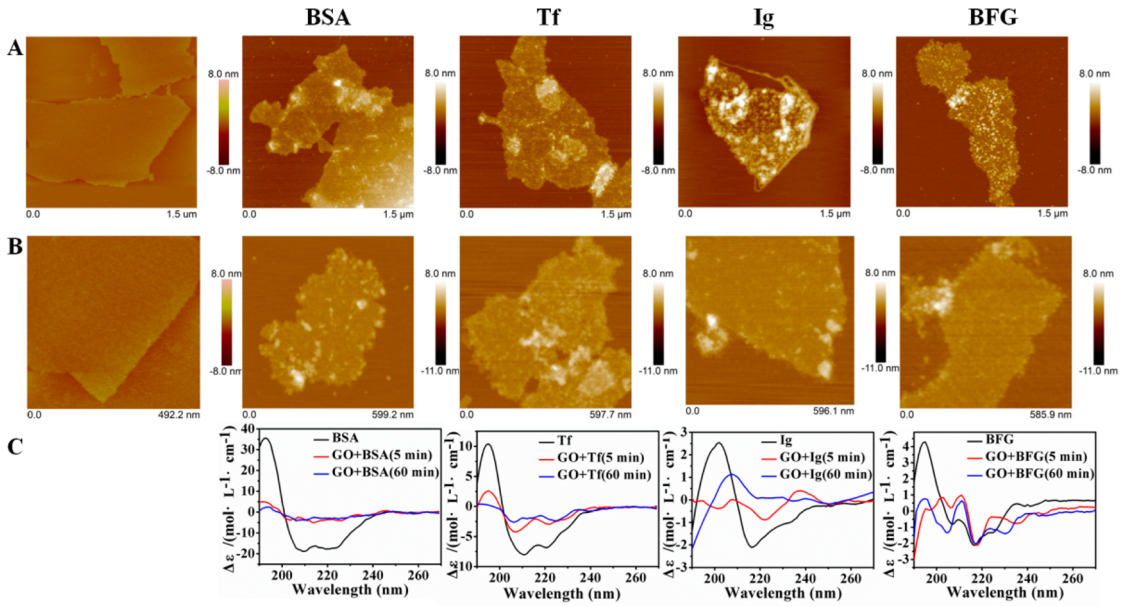

Figure 3. Interactions between BSA, Tf, IgG, BFG, and GO, as illustrated by AFM. AFM images of bare-GO (first column) and protein complexes are shown after incubation with GO for 5 min (A) and 60 min (B).Corresponding CD spectra of the resulting protein aggregates are shown in panel (C).

processes. It should be noted that pristine graphene was chosen here for the MD simulations, while GO and rGO were used in the experiments due to the poor water solubility of pristine graphene. However, in our previous study of the graphene interaction with *E. coli* cell membranes,[42] we did simulate GO nanosheets using the Lerf–Klinowski model ($C_{10}O_1(OH)_1(COOH)_{0.5}$) as well, which represents the typical outcome from the graphene oxidation.[55−57] The simulation results from GO nanosheets were largely consistent with those from pristine graphene counterparts, with only slightly less intensity in their interactions with cell membranes.[42] It is also interesting to note that large unoxidized residual graphene-like regions can exist on GO nanosheets (the so-called "sp^2-domain"),[55,58,59] with up to ~60% of the surface remaining undisturbed.[58] For rGOs, this large sp^2-domain will be particularly the case, with only ~3% the oxygen content. Thus, in the current simulation studies, we used pristine graphene to mimic this sp^2-domain of GOs and rGOs.

An illustrative example of the latter is shown in Figure 4, where snapshots at different simulation times of the adsorption of BFG are depicted. Among the four proteins under consideration, BFG is by far the most voluminous, meaning that, in principle, BFG simulations should provide an upper limit for the time required to achieve adsorption over this set of systems. Interestingly, initial BFG contacts are readily observed at around 20 ns in our MD simulation trajectory, followed by structural rearrangements that seem to be driven by hydrophobic interactions (see Figure 4, the 170 ns snapshot). In particular, the orientations of aromatics rings corresponding to Trp, Tyr, and Phe align with the graphene surface (see Figure 4) to facilitate $\pi-\pi$ stacking between the respective conjugated systems.[52,60] Furthermore, positive correlations

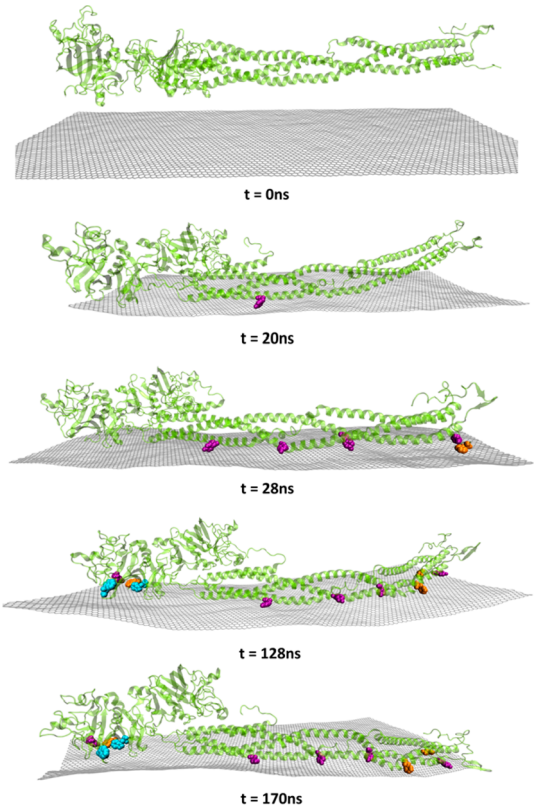

Figure 4. Representative molecular dynamics snapshots of the absorption of BFG onto the graphene surface. Cartoon representations of the full protein are depicted in yellow, and hydrophobic Tyr (purple), Phe (orange), and Trp (blue) within 0.5 nm distance of the graphene surface are represented as vdW spheres. Atoms corresponding to the graphene sheet are colored in gray.

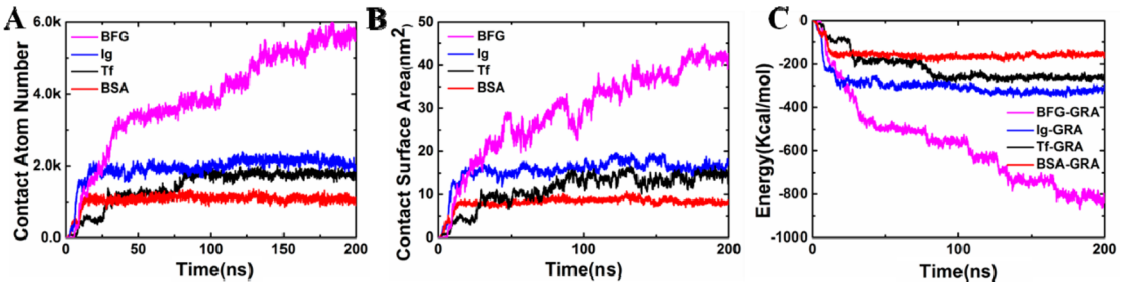

Figure 5. Time-series of the adsorption descriptors in MD simulations: (A) the contact atom number; (B) the contact surface area; and(C) the pair interaction energy between the proteins and graphene.

between adsorption capacity and characteristics like protein molecular weight, hydrophobic residue content, and Trp, Tyr, and Phe residual content exists (Supporting Information Figure S4), confirming the above observation. These correlations indicate that not only surface atoms are involved in the adsorption phenomenon, but buried residues as well once the protein partially unfolds on the graphene surface. The latter is particularly clear for BFG (see next paragraph). To further study the underlying molecular mechanisms of BSA adsorption, some critical intermediate states were carefully examined. As shown in Supporting Information Figure S5, at $t = 12.8$ ns, a small drying zone emerged at the interface between residues Ala-583, Ala-584, and graphene, in which all water molecules originally resided there were expelled. Subsequently, at $t = 16.8$ ns, the drying zone expanded to a larger interface region between graphene and a hydrophobic cluster, which consists of residues Phe-574, Ala-576, Phe-577, and Val-578. From 16.8 to 20 ns, the drying region spread to a much larger area, consisting additional hydrophobic residues of Phe-416, Leu-421, Tyr-424, Phe-426, Ala-429, Met-571, Val-575, and Leu-567. These results suggest that the drying phenomena also plays an important role in the adsorption of BSA onto the surface of graphene, a process that has been previously described in the literature.[61] Interestingly, water molecules located in-between BSA hydrophilic regions and graphene persisted throughout the entire simulation time; in other words, these water molecules act as a lubricant for the binding of BSA hydrophilic regions onto the graphene.

The adsorption processes for all four proteins were monitored using three dynamical parameters: (1) the contact atom number (CAN), defined as the total number of heavy atoms within a 0.5 nm distance of the graphene surface; (2) the contact surface area (CSA), defined as the difference between the whole solvent-accessible surface area (SASA) of the free protein and the partial SASA of exposed protein in the protein−GO complex; and (3) the total pair interaction energy between the protein and graphene. The time series of these three descriptors are illustrated in Figure 5, panels A, B, and C, respectively. The CANs and CSAs (Figure 5A,B) are in line with previous results concerning protein adsorption on SWCNTs,[52] reaching an approximate steady-state in Ig, Tf, and BSA at around 100, 75, and 10 ns, respectively. In turn, BFG never truly reaches steady-state conditions, perhaps due to further conformational rearrangements that occur to accommodate buried hydrophobic residues on the surface of the nanosheet. The heterogeneous nature of CD spectra BFG (see Figure 3) support our simulation-based observations of slowed equilibration in this particular system. Not surprisingly, the pair interaction energies follows a similar trend, with favorable energies deepening with the increment of protein hydrophobicity (see Supporting Information Figure S5). A decomposition of the total protein interaction energy into contributions arising from graphene ("GRA"), water ("solv"), and ions ("rest") is presented in Figure 6. Particularly noteworthy are the large magnitudes of "protein-GRA" components in BFG and Ig (van der Waals interactions or dispersion interactions), given their statistical equivalence to concomitant "protein-solv" interaction energies: clearly, these two proteins exhibit highly hydrophobic characteristics. To some extent, this adsorption and packing of proteins like BFG onto graphene is reminiscent of the hydrophobic collapse of protein complexes during their folding.[54,62−64] Meanwhile, the "protein-rest" interactions are also enhanced in all four systems over time, implying that polar and charged residues become more exposed to dissolved ions during the adsorption process. If GO were used in simulations, the electrostatic portion of the "protein-GRA" interactions would be enhanced somewhat due to the oxidation-induced charges on hydroxyl, epoxyl, and carbonyl groups on GO surfaces, but because of the existence of large sp_2-domains on GOs and rGOs,[55,58,59] the $\pi-\pi$ stacking and hydrophobic interactions are believed to still play a dominant role, particularly for rGOs.

On the basis of these results, our MD simulations predict a binding strength in full accordance with the experimental results presented in previous sections (BFG > Ig > Tf > BSA). Interestingly, positive correlations exist between molecular weights, the number of hydrophobic residues, and the aromatic residues content with the adsorption capacity (see Supporting Information Figure S3). The strong correspondence between binding energies and measured capacities suggests that relative binding affinities are enthalpically driven.

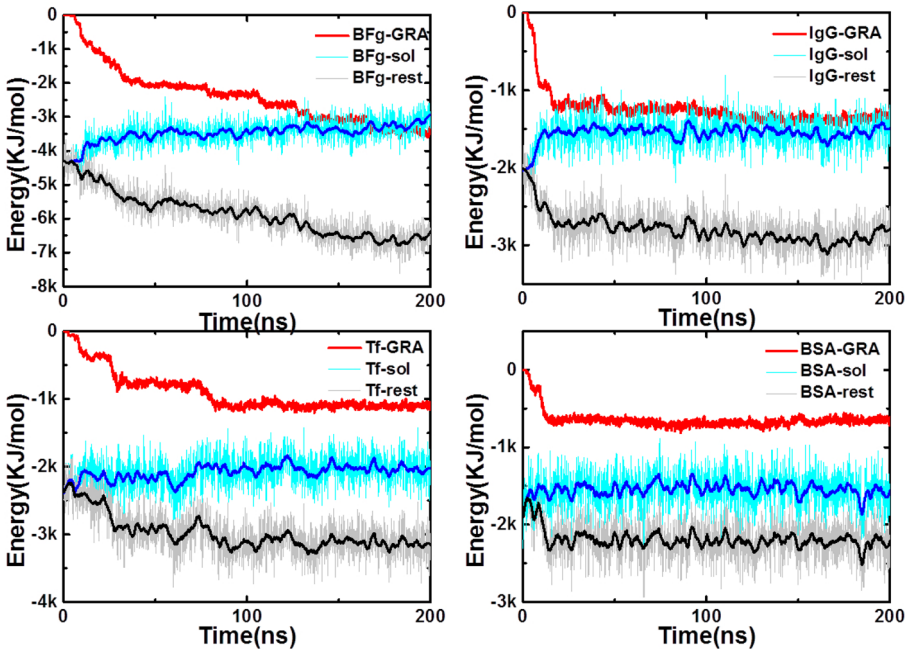

Figure 6. Time-series of the different contributions to the total solvation energy of the proteins: Graphene ("GRA"), water ("solv"), and ions ("rest").

More importantly, the above results point toward a similar mechanism for protein−GO interactions as compared to protein−SWCNT interactions. Indeed, the CSAs shown in Figure 5 are only slightly higher than those reported for SWCNTs,[52] implying that the enhanced adsorption capacity of GO (rGO) is not because of a notorious difference on the interaction mode between the protein and GO (rGO), but due to the increment of the available surface-area of GO nanosheets. Nevertheless, it is important to note that the simulated times herein are orders of magnitude shorter than the experimentally observed times for adsorption (see Figure 1D,E). More drastic conformational changes that might occur at longer times cannot be discarded, as the CD data for BFG and Ig, in particular, portend (see Figure 3). Indeed, previous longer simulations (5×1 ms) of BFG with SWCNT also indicate that the flexible long helical tails of BFG protein can wrap onto the SWCNT to form tight complexes.[65]

Cytotoxicity. On the basis of our newfound understanding of interactions between GO nanosheets and serum proteins, we carried out an *in vitro* experiment to evaluate whether protein coatings on GO surfaces mitigate the cytotoxicity of GO and compare this effect relative to that of SWCNTs. As mentioned above, GO presents a consistent ordering of adsorption capacities for the studied proteins, that is BFG > Ig > Tf > BSA. To strongly demonstrate that protein coating can effectively reduce the cytotoxicity of GO, a protein with the lowest adsorption capacity (and weakest affinity), *i.e.*, BSA, was chosen in this study. First, A549 cells were incubated in complete culture medium containing 10% FBS. After 24 h incubation, the viability of A549 cells reached ~80% confluence. Then, these A549 cells were separately treated with pristine GO sheets and SWCNTs for another 24 h in serum-free medium (0% FBS). As shown in Figure 7A, cell viability exposed to GO sheets (200 μg/mL) was determined to be ~55%, well above the value of ~10% observed for SWCNTs at the same concentration. Even at greatly reduced SWCNT concentrations (15 μg/mL), cell viability was still only found to be in the neighborhood of 50%. When subjected to preincubation with BSA, GO nanosheets and SWCNT again exhibited extremely discrepant levels of cytotoxicity. Precoated SWCNTs were slightly less detrimental to cell viability than their pristine counterparts (offering a viability improvement of less than 5%); by contrast, BSA-coated GO sheets showed almost no cytotoxicity. In general, the higher the adsorption capacity, the stronger the reduction in toxicity, as shown in our previous study on SWCNT with the same four serum proteins.[52] The experimental results also confirmed that the cell toxicity induced by uncoated GO was almost completely eliminated after GO coating with other three serum proteins (Supporting Information Figure S6). Similar trends were observed in the fluorescence-based LIVE/DEAD assays illustrated in Figure 7B and Supporting Information Figure S7. Further measurements of cell viability after exposure to GO, BSA-GO, SWCNTs, and BSA-SWCNT in a 10% serum protein medium (10% FBS) show the same trend. As shown in Figure 7, GO nanosheets once again exhibited almost no cytotoxicity after 10% FBS exposure, both when pretreated with BSA and when left untreated; however, the addition of the FBS medium did not significantly reduce the cytotoxicity of SWCNTs.

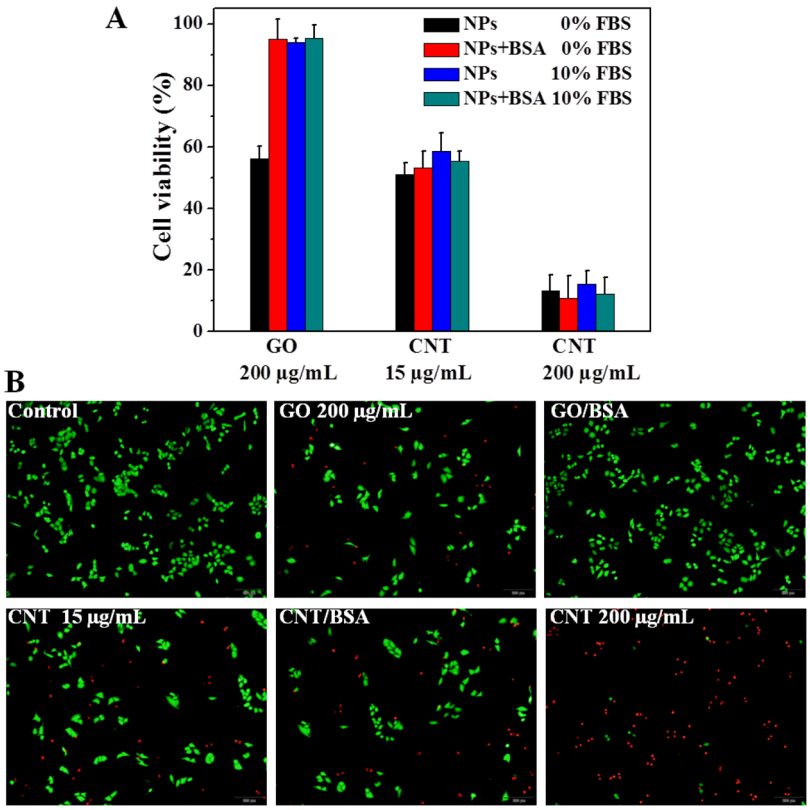

Figure 7. Effects of GO/SWCNTs with and without serum protein coatings on cell proliferation. Differential cytotoxicities in the presence and absence of FBS buffer are presented at top (A); images of live and dead stains (B) of A549 cells exposed to nanoparticles with/without protein coatings for 24 h are shown at bottom.

In perspective, the strong protein−GO interactions brought fast and remarkable adsorption of protein onto the surface of GO nanosheets, which impede the cellular uptake and cell membrane adhesion of GO nanosheets, thereby the dramatic reduction in cytotoxicity. Conversely, the less marked interactions between SWCNTs and serum proteins brought moderate adsorption of protein onto the surface of SWCNT and lead to little attenuation in the cellular uptake and surface adhesion of the nanoparticles in question.

CONCLUSION

In this work, we have used comprehensive experimental and simulation-based techniques to characterize the adsorption of four serum proteins onto graphene oxide (GO) and reduced GO (rGO) nanosheets. Binding affinities follow the rank order (BFG > Ig > Tf > BSA), which was predicted by molecular dynamics data and confirmed by a variety of experimental results. In general, GO is observed to exhibit a greatly enhanced protein adsorption capacity over one-dimensional SWCNTs. Simulations suggest that hydrophobic interactions and, in particular, $\pi-\pi$ stacking interactions, between proteins and the GO surface are essential to strong adsorption of protein molecules. Such binding mode characteristics are consistent with previous observations of protein-SWCNT interactions, implying that the augmented adsorptive capacity of GO/rGO can be attributed to the flat binding surface offered by planar graphene derivatives. Interestingly, the basis for GO-induced cytotoxicity is thought to reside in the membrane cutting and extraction of individual phospholipid chains from cell membranes.[42] Thus, it is not unreasonable to propose that protein-coated GO sheets lack the capacity for such cutting and destructive extractions due to the obvious increase in the "thickness" and reduction of the available surface area of GO, instead brandishing largely hydrophilic exteriors that lead to benign interactions with phospholipid head groups. Other possible mechanisms including the suppression of redox activity and lysosomal disruption might also be in play. Similar physical considerations likely govern the cytotoxicity of a wide range of hydrophobic nanomaterials. To gauge the applicability of such considerations in other biological contexts, however, the details of particular protein−nanoparticle interactions must be well understood. Proteins exist in considerable quantity and diversity in biological fluids, and given their lack of evolutionary optimization alongside artificial nanomaterials, such proteins will exhibit nonspecific and generally complicated interactions with synthetic substrates. As nanoscale devices become more and more prevalent in biomedical applications, physicists and medical practitioners alike must carefully monitor

protein−nanomaterial interactions. In the case of GO, cooperation between physics and medicine has revealed a promising candidate material for use in nanotherapies of the future.

MATERIALS AND METHODS

Materials. Graphene oxide (GO, with lateral dimension 0.5−3 μm), reduced graphene oxide (rGO, with lateral dimension 0.5−3 μm) and ultra high-purity single-wall carbon nanotubes (SWCNTs, purity >95 wt %, outer diameter <2 nm, and 5−30 μm in length) were purchased from Chengdu Organic Chemical Company, Chinese Academy of Science. Bovine serum albumin (BSA), transferrin (Tf), fibrinogen (BfG), and immunoglobulin (Ig) were obtained from Sigma-Aldrich. Fetal bovine serum (FBS), and the LIVE/DEAD viability/cytotoxicity kit were purchased from Invitrogen. The CCK-8 assay kit was obtained from Dojindo Laboratories.

Adsorption Capacity and Adsorption Kinetics. Protein intrinsic fluorescence, with excitation and emission wavelengths of 280 and 332 nm, respectively, was used to track the adsorption process of proteins onto nanoparticle surfaces. In brief, nanoparticle suspensions (including GO, rGO and SWCNT) were prepared by dispersing nanoparticle powders in pure water. Protein solutions ranging from 0.2 to 3.2 mg/mL were prepared in standard phosphate buffer saline (PBS). Subsequently, nanoparticle suspensions were mixed with an equal volume of protein solution and constantly shaken for 24 h at 37 C prior to centrifugation at 14 800*g* for 10 min. After discarding the sediments, the contents of free protein in supernatant were measured *via* fluorescence spectroscopy. On the basis of the above results, saturating protein concentrations were chosen in order to study adsorption kinetics. Nanoparticle suspensions were mixed with protein solutions and incubated for different time intervals (0, 5, 30, 60, 120, 240, 360 min). Likewise, the fraction of bound protein was monitored by measuring the fluorescence intensity of the remaining protein in the supernatant.

In view of the content of adsorbed protein, it is possibly correlated with specific surface area of nanomaterials, which are measured using BET and AFM. Specific surface area of GO can be roughly estimated as 2600 m^2/g according to the average height of 0.8 nm based on the AFM images (Figure 3 A). Meanwhile about 1−10 stacks graphene sheets can be developed with an average specific surface area of ~574 m^2/g of rGO. For CNT, the specific surface area is 419 m^2/g from BET measurement. As a further GO/rGO characterization, we can also replot the amount of adsorbed proteins with normalized specific surface area (*i.e.*, mg-protein/m^2-nanomaterial) for the three nanomaterials with four proteins (see Supporting Information Figure S8). On all cases, the nanomaterials present a consistent ordering of adsorption capacities for the studied proteins, that is BFG > Ig > Tf > BSA. Moreover, the adsorption capacities of GO and rGO still are much higher than those of SWCNTs, so the conclusion that proteins prefer the flat surfaces of graphene to the curved surfaces of CNTs should be reliable. In addition, rGO is seen to be a more effective sorbent than GO with this renormalization, which is consistent with, and supports, the idea that $\pi-\pi$ interactions and hydrophobic interactions are primary driving forces.

Characterization of GO−Protein Conjugates by Atomic Force Microscopy (AFM). Protein solutions were mixed with equal volumes of GO sheet suspensions previously shaken for 5 and 60 min at 37 C. The GO−protein conjugates were deposited on the surface of freshly cleaved mica, rinsed with distilled water, and vacuum-dried at room temperature. Image data was acquired and analyzed using an AFM (Nanoscope Icon, Veeco) in tapping mode.

Protein Secondary Structure Determination *via* Circular Dichroism (CD). Samples were prepared by mixing protein solutions with equal volumes of GO sheets solutions (100 μg/mL); free GO solutions were used as negative controls. All of the samples were shaken at 37 °C for 5 or 60 min. CD spectra were recorded on a JASCO J-810, Japan instrument using quartz cells with a path length of 10 mm. The resulting spectra were corrected by subtracting the background signal of GO.

Surface Plasmon Resonance (SPR) Affinity Measurements. OctetRED96 (ForteBio) SPR equipment was used to quantitatively characterize binding interactions between GO sheets and protein. The total working volume for samples or buffer was 200 μL per well with an agitated speed of 1000 rpm. Streptavidin (SA) biosensor tips were prewetted for at least 5 min in distilled water immediately prior to the assay. Afterward, GO sheets were noncovalently loaded to saturation onto the SA tips. Negative controls were prepared using the same loading process without the addition of the nanoparticle solutions. GO loaded tips were washed in PBS for balance and transferred to wells containing different concentrations of protein. Associations were measured for about 300 s and dissociations were monitored until equilibrium was reached. The kinetic parameters (K_{on} and K_{off}) and dissociation constants (K_D) were calculated using the Octet software.

***In Vitro* Cytotoxicity.** Cellular viability was evaluated with CCK-8 assay kits (Dojindo Corp, Japan). Briefly, A549 cells were seeded on 96-well plates (Corning) at a density of 5000 cells per well, and cultured in complete culture medium containing 10% FBS. After 24 h incubation, A549 cells reached ~80% confluence. Subsequently, the medium was replaced by pristine nanoparticles and protein-bound nanoparticle dispersions, freshly prepared by diluting the nanoparticle stock in serum-free DMEM/F12 or medium supplemented with 10% FBS for 24 h. Cells cultured without nanoparticles were taken as the negative control. CCK-8 reagent was added to the cells 2 h before measuring the optical density (OD) by a microplate reader (Synergy NEO HTS, Biotek) at 450 nm.

Live/Dead Viability/Cytotoxicity Assay. To further verify the results in CCK-8 assay, cells were staining using a LIVE/DEAD Viability/Cytotoxicity Kit (Invitrogen) according to the manufacturer's protocol. A549 cells were treated with pristine nanoparticles and protein-bound nanoparticles for 24 h. The cells were washed with serum-free buffer, followed by the addition of 1 mL of PBS containing 2 μL of ethidium homodimer-1 and 0.4 μL of Calcein AM. The labeled cells were analyzed by fluorescence microscopy (Olympus, Japan) after 30 min of incubation.

Computational Methods. The starting 3D structures of BFG, Ig, and Tf were obtained from the Protein Data Bank (PDB)[66] with PDB entry codes 1DEQ,[67] 3HR5,[68] and 2HAV,[69] respectively. BSA was modeled *via* an homology model from the Swiss-Model Repository,[70] SWISS-MODEL ID 432779d395a52bfc9f6574bc3e98afcd_1. In particular for BFG, the P4, P5, and P6 chains were chosen with modified groups ignored. In the case of Ig, only one heavy and one light chain were used. Hydrogens and any other missing atom were added based on the internal coordinates definitions of the CHARMM topology files.[71] Graphene sheets were generated *via* the nanotube builder plugin of the VMD software package.[72] The resulting size of the graphene sheets were 25.7 × 10.1 nm^2 for BFG, 9.8 × 7.1 nm^2 for Ig, 9.8 × 9.2 nm^2 for Tf, and 9.8 × 10.1 nm^2 for BSA. Energetically minimized and relaxed structures for both the protein and the graphene sheet were placed in a cubic box and placed at a minimum distance of 1.0 nm between any heavy atom of the protein and the sheet surface. The box was enlarged to add a distance of 1.5 nm around the complex and solvated with water. Na^+ or Cl^- ions were added in order to electrically neutralize the BFG, Ig, Tf, and BSA systems. This resulted in simulation boxes containing 612 464, 217 581, 270 888, and 217 519 atoms for the BFG, Ig, Tf, and BSA systems, respectively. The TIP3P model[73] was adopted for water, while the CHARMM27 potential energy function[71] was used for the proteins. The graphene carbon atoms were modeled as uncharged Lenard-Jones particles with a cross-section of s_{cc} = 0.34 nm and a depth of the potential well of e_{cc} = 0.3598 kJ mol^{-1}. Carbon−carbon bond lengths and bond angles were maintained by harmonic potentials with spring constants of 392 460 kJ mol^{-1} nm^{-2} and

527 kJ mol^{-1} rad^{-2}, respectively. Molecular dynamics (MD) simulations were carried out using the GROMACS v 4.6.3 package74. The VMD and Chimera software suites were used for trajectory visualization and analysis. Constant temperature (at 310 K) and pressure (at 1 atm) were maintained by using a v-rescale thermostat[75] and the Parrinello−Rahmann pressure coupling method.[76] Periodic boundary conditions were applied in all directions. The particle-mesh Ewald method was used to treat long-range electrostatic interactions,[77] whereas the vdW interactions were treated with a cutoff distance of 1.2 nm. LINCS[78] was applied to constrain bond lengths within the solute, whereas the analytical SETTLE algorithm[79] was employed to maintain the rigidity of the TIP3P model. Before production runs, short 1 ns NVT simulations with the graphene nanosheet and protein positionally restrained were performed in order to equilibrate the solvent molecules around the solute. Each system was then simulated in the NPT ensemble (fixed number of atoms N, pressure P, and temperature T) for 200 ns.

In a previous work, we examined the effects of softness and surface curvature of graphene on its interaction with protein HP35, finding that it influences the protein adsorption specifically enhancing stacking interactions.[80] Thus, in the current simulation, a fully flexible GO surface was used in order to account for such effects.

Conflict of Interest: The authors declare no competing financial interest.

Acknowledgment. We thank Bruce Berne, Zhifang Chai, Yuliang Zhao, Seung-gu Kang, Chunying Chen, and Andre Nel for helpful discussions. This work was partially supported by the National Natural Science Foundation of China under Grant Nos. 11374221, 21320102003, 21207164 the National Basic Research Program of China (2014CB931900). J.A.G. acknowledges financial support from the Fondo Nacional de Desarrollo Cientfico y Tecnologico (FONDECYT) project number 3130547 and project ACT-1107 PIA-CONICYT. R.Z. acknowledges the support from IBM Blue Gene Science Program. A Project Funded by the Priority Academic Program Development of Jiangsu Higher Education Institutions (PAPD), and Jiangsu Provincial Key Laboratory of Radiation Medicine and Protection, as well as the Graduate Education Innovation Program of Jiangsu Province (KYZZ_0343), the Fundamental Research Funds for the Central Universities. R.Z. conceived and designed the simulations and experiments. Z.Y., Z.G., and J.L. performed the simulations. Y.C. and C.G. carried out the experiments. R.Z., Z.Y., C.G., Y.C., J.A.G., Z. G. and J.K.W. analyzed the data. J.A.G., C.G., Z.Y., J. K.W. and R.Z. cowrote the paper.

Supporting Information Available: GO sheets properties; protein adsorption capacity of GO, rGO and SWCNTs in 2% and 4% FBS; SDS−PAGE analysis of interaction between GO and individual protein; AFM images of native proteins; AFM images of native proteins; analysis of protein residue contents and their correlation with the protein adsorption capacity on nanoparticles; representative trajectory snapshots of the water dynamics during the adsorption of BSA onto the surface of graphene nanosheet; cell viability of A549 cells; effects of GO/SWCNTs with and without serum protein coatings on cell proliferation; AFM images of rGO. The Supporting Information is available free of charge on the ACS Publications website at DOI: 10.1021/nn5066606.

REFERENCES AND NOTES

1. Michalet, X.; Pinaud, F. F.; Bentolila, L. A.; Tsay, J. M.; Doose, S.; Li, J. J.; Sundaresan, G.; Wu, A. M.; Gambhir, S. S.; Weiss, S. Quantum Dots for Live Cells, *in Vivo* Imaging, and Diagnostics. *Science* **2005**, *307*, 538–544.
2. Rosi, N. L.; Giljohann, D. A.; Thaxton, C. S.; Lytton-Jean, A. K. R.; Han, M. S.; Mirkin, C. A. Oligonucleotide-Modified Gold Nanoparticles for Intracellular Gene Regulation. *Science* **2006**, *312*, 1027–1030.
3. Grossman, J. H.; McNeil, S. E. Nanotechnology in Cancer Medicine. *Phys. Today* **2012**, *65*, 38–42.
4. Mundra, R. V.; Wu, X.; Sauer, J.; Dordick, J. S.; Kane, R. S. Nanotubes in Biological Applications. *Curr. Opin. Biotechnol.* **2014**, *28*, 25–32.
5. Iijima, S. Helical Microtubules of Graphitic Carbon. *Nature* **1991**, *354*, 56–58.
6. Snow, E. S.; Perkins, F. K.; Houser, E. J.; Badescu, S. C.; Reinecke, T. L. Chemical Detection with a Single-Walled Carbon Nanotube Capacitor. *Science* **2005**, *307*, 1942–1945.
7. Hinds, B. J.; Chopra, N.; Rantell, T.; Andrews, R.; Gavalas, V.; Bachas, L. G. Aligned Multiwalled Carbon Nanotube Membranes. *Science* **2004**, *303*, 62–65.
8. Singh, R.; Pantarotto, D.; Lacerda, L.; Pastorin, G.; Klumpp, C.; Prato, M.; Bianco, A.; Kostarelos, K. Tissue Biodistribution and Blood Clearance Rates of Intravenously Administered Carbon Nanotube Radiotracers. *Proc. Natl. Acad. Sci. U.S.A.* **2006**, *103*, 3357–3362.
9. Liu, Z.; Sun, X.; Nakayama-Ratchford, N.; Dai, H. Supramolecular Chemistry on Water-Soluble Carbon Nanotubes for Drug Loading and Delivery. *ACS Nano* **2007**, *1*, 50–56.
10. Heister, E.; Neves, V.; Lamprecht, C.; Silva, S. R. P.; Coley, H. M.; McFadden, J. Drug Loading, Dispersion Stability, and Therapeutic Efficacy in Targeted Drug Delivery with Carbon Nanotubes. *Carbon* **2012**, *50*, 622–632.
11. Liu, Z.; Chen, K.; Davis, C.; Sherlock, S.; Cao, Q.; Chen, X.; Dai, H. Drug Delivery with Carbon Nanotubes for *in Vivo* Cancer Treatment. *Cancer Res.* **2008**, *68*, 6652–6660.
12. Moon, H. K.; Lee, S. H.; Choi, H. C. *In vivo* near-Infrared Mediated Tumor Destruction by Photothermal Effect of Carbon Nanotubes. *ACS Nano* **2009**, *3*, 3707–3713.
13. Robinson, J. T.; Welsher, K.; Tabakman, S. M.; Sherlock, S. P.; Wang, H.; Luong, R.; Dai, H. High Performance *in Vivo* near-IR (>1 Mm) Imaging and Photothermal Cancer Therapy with Carbon Nanotubes. *Nano Res.* **2010**, *3*, 779–793.
14. Bardhan, N. M.; Ghosh, D.; Belcher, A. M. Carbon Nanotubes as *in Vivo* Bacterial Probes. *Nat. Commun.* **2014**, *5*, 4918–4928.
15. Geim, A. K. Graphene: Status and Prospects. *Science* **2009**, *324*, 1530–1534.
16. Schwierz, F. Graphene Transistors. *Nat. Nanotechnol.* **2010**, *5*, 487–496.
17. Sreekanth, K. V.; Zeng, S.; Shang, J.; Yong, K.-T.; Yu, T. Excitation of Surface Electromagnetic Waves in a Graphene-Based Bragg Grating. *Sci. Rep.* **2012**, *2*, 737–743.
18. Kürüm, U.; Ekiz, O. O.; Yaglioglu, H. G.; Elmali, A.; Urel, M.; Güner, H.; Mizrak, A. K.; Ortaç, B.; Dâna, A. Electrochemically Tunable Ultrafast Optical Response of Graphene Oxide. *Appl. Phys. Lett.* **2011**, *98*, 141103.
19. Feng, L.; Liu, Z. Graphene in Biomedicine: Opportunities and Challenges. *Nanomedicine* **2011**, *6*, 317–324.
20. Sanchez, V. C.; Jachak, A.; Hurt, R. H.; Kane, A. B. Biological Interactions of Graphene-Family Nanomaterials: An Interdisciplinary Review. *Chem. Res. Toxicol.* **2012**, *25*, 15–34.
21. Yang, K.; Zhang, S.; Zhang, G.; Sun, X.; Lee, S. T.; Liu, Z. Graphene in Mice: Ultrahigh *in Vivo* Tumor Uptake and Efficient Photothermal Therapy. *Nano Lett.* **2010**, *10*, 3318–3323.
22. Okada, F. Beyond Foreign-Body-Induced Carcinogenesis: Impact of Reactive Oxygen Species Derived from Inflammatory Cells in Tumorigenic Conversion and Tumor Progression. *Int. J. Cancer.* **2007**, *121*, 2364–2372.
23. Soldano, C.; Mahmood, A.; Dujardin, E. Production, Properties and Potential of Graphene. *Carbon* **2010**, *48*, 2127–2150.
24. Chang, Y.; Yang, S.-T.; Liu, J.-H.; Dong, E.; Wang, Y.; Cao, A.; Liu, Y.; Wang, H. *In Vitro* Toxicity Evaluation of Graphene Oxide on A549 Cells. *Toxicol. Lett.* **2011**, *200*, 201–210.
25. Zhang, Y.; Ali, S. F.; Dervishi, E.; Xu, Y.; Li, Z.; Casciano, D.; Biris, A. S. Cytotoxicity Effects of Graphene and Single-Wall Carbon Nanotubes in Neural Phaeochromocytoma-Derived pc12 Cells. *ACS Nano* **2010**, *4*, 3181–3186.
26. Yang, K.; Wan, J.; Zhang, S.; Zhang, Y.; Lee, S. T.; Liu, Z. *In Vivo* Pharmacokinetics, Long-Term Biodistribution, and Toxicology of Pegylated Graphene in Mice. *ACS Nano* **2011**, *5*, 516–522.

27. Li, Y.; Liu, Y.; Fu, Y.; Wei, T.; Le Guyader, L.; Gao, G.; Liu, R. S.; Chang, Y. Z.; Chen, C. The Triggering of Apoptosis in Macrophages by Pristine Graphene through the MAPK and TGF-Beta Signaling Pathways. *Biomaterials* **2012**, *33*, 402–411.
28. Zhang, W.; Wang, C.; Li, Z.; Lu, Z.; Li, Y.; Yin, J. J.; Zhou, Y. T.; Gao, X.; Fang, Y.; Nie, G.; et al. Unraveling Stress-Induced Toxicity Properties of Graphene Oxide and the Underlying Mechanism. *Adv. Mater.* **2012**, *24*, 5391–5397.
29. Zhao, Y.; Xing, G.; Chai, Z. Nanotoxicology: Are Carbon Nanotubes Safe? *Nat. Nanotechnol.* **2008**, *3*, 191–192.
30. Nel, A.; Xia, T.; Mädler, L.; Li, N. Toxic Potential of Materials at the Nanolevel. *Science* **2006**, *311*, 622–627.
31. Nel, A. E.; Mädler, L.; Velegol, D.; Xia, T.; Hoek, E. M. V; Somasundaran, P.; Klaessig, F.; Castranova, V.; Thompson, M. Understanding Biophysicochemical Interactions at the Nano-Bio Interface. *Nat. Mater.* **2009**, *8*, 543–557.
32. Yang, K.; Ma, Y.-Q. Computer Simulation of the Translocation of Nanoparticles with Different Shapes across a Lipid Bilayer. *Nat. Nanotechnol.* **2010**, *5*, 579–583.
33. Shi, X.; von dem Bussche, A.; Hurt, R. H.; Kane, A. B.; Gao, H. Cell Entry of One-Dimensional Nanomaterials Occurs by Tip Recognition and Rotation. *Nat. Nanotechnol.* **2011**, *6*, 714–719.
34. Vácha, R.; Martinez-Veracoechea, F. J.; Frenkel, D. Receptor-Mediated Endocytosis of Nanoparticles of Various Shapes. *Nano Lett.* **2011**, *11*, 5391–5395.
35. Salvador-Morales, C.; Townsend, P.; Flahaut, E.; Vénien-Bryan, C.; Vlandas, A.; Green, M. L. H.; Sim, R. B. Binding of Pulmonary Surfactant Proteins to Carbon Nanotubes; Potential for Damage to Lung Immune Defense Mechanisms. *Carbon* **2007**, *45*, 607–617.
36. Linse, S.; Cabaleiro-Lago, C.; Xue, W.-F.; Lynch, I.; Lindman, S.; Thulin, E.; Radford, S. E.; Dawson, K. A. Nucleation of Protein Fibrillation by Nanoparticles. *Proc. Natl. Acad. Sci. U.S.A.* **2007**, *104*, 8691–8696.
37. Lundqvist, M.; Stigler, J.; Elia, G.; Lynch, I.; Cedervall, T.; Dawson, K. A. Nanoparticle Size and Surface Properties Determine the Protein Corona with Possible Implications for Biological Impacts. *Proc. Natl. Acad. Sci. U.S.A.* **2008**, *105*, 14265–14270.
38. Hu, W.; Peng, C.; Luo, W.; Lv, M.; Li, X.; Li, D.; Huang, Q.; Fan, C. Graphene-Based Antibacterial Paper. *ACS Nano* **2010**, *4*, 4317–4323.
39. Akhavan, O.; Ghaderi, E. Toxicity of Graphene and Graphene Oxide Nanowalls against Bacteria. *ACS Nano* **2010**, *4*, 5731–5736.
40. Liu, S.; Zeng, T. H.; Hofmann, M.; Burcombe, E.; Wei, J.; Jiang, R.; Kong, J.; Chen, Y. Antibacterial Activity of Graphite, Graphite Oxide, Graphene Oxide, and Reduced Graphene Oxide: Membrane and Oxidative Stress. *ACS Nano* **2011**, *5*, 6971–6980.
41. Krishnamoorthy, K.; Veerapandian, M.; Zhang, L. H.; Yun, K.; Kim, S. J. Antibacterial Efficiency of Graphene Nanosheets against Pathogenic Bacteria *via* Lipid Peroxidation. *J. Phys. Chem. C* **2012**, *116*, 17280–17287.
42. Tu, Y.; Lv, M.; Xiu, P.; Huynh, T.; Zhang, M.; Castelli, M.; Liu, Z.; Huang, Q.; Fan, C.; Fang, H.; et al. Destructive Extraction of Phospholipids from Escherichia Coli Membranes by Graphene Nanosheets. *Nat. Nanotechnol.* **2013**, *8*, 594–601.
43. Li, Y.; Feng, L.; Shi, X.; Wang, X.; Yang, Y.; Yang, K.; Liu, T.; Yang, G.; Liu, Z. Surface Coating-Dependent Cytotoxicity and Degradation of Graphene Derivatives: Towards the Design of Non-Toxic, Degradable Nano-Graphene. *Small* **2014**, *10*, 1544–1554.
44. Zhang, Y.; Wu, C.; Guo, S.; Zhang, J. Interactions of Graphene and Graphene Oxide with Proteins and Peptides. *Nanotechnol. Rev.* **2013**, *2*, 27–45.
45. Mu, Q.; Su, G.; Li, L.; Gilbertson, B. O.; Yu, L. H.; Zhang, Q.; Sun, Y. P.; Yan, B. Size-Dependent Cell Uptake of Protein-Coated Graphene Oxide Nanosheets. *ACS Appl. Mater. Interfaces* **2012**, *4*, 2259–2266.
46. Hu, W.; Peng, C.; Lv, M.; Li, X.; Zhang, Y.; Chen, N.; Fan, C.; Huang, Q. Protein Corona-Mediated Mitigation of Cytotoxicity of Graphene Oxide. *ACS Nano* **2011**, *5*, 3693–3700.
47. Lesniak, A.; Fenaroli, F.; Monopoli, M. P.; Åberg, C.; Dawson, K. A.; Salvati, A. Effects of the Presence or Absence of a Protein Corona on Silica Nanoparticle Uptake and Impact on Cells. *ACS Nano* **2012**, *6*, 5845–5857.
48. Lesniak, A.; Salvati, A.; Santos-Martinez, M. J.; Radomski, M. W.; Dawson, K. A.; Åberg, C. Nanoparticle Adhesion to the Cell Membrane and Its Effect on Nanoparticle Uptake Efficiency. *J. Am. Chem. Soc.* **2013**, *135*, 1438–1444.
49. Zhang, Y.; Wu, C.; Guo, S.; Zhang, J. Interactions of graphene and graphene oxide with proteins and peptides. *Nanotechnol Rev.* **2013**, *2*, 27–45.
50. Ding, Z.; Ma, H.; Chen, Y. Interaction of Graphene Oxide with Human Serum Albumin and Its Mechanism. *RSC Adv.* **2014**, *4*, 55290–55295.
51. Kim, J. A.; Salvati, A.; Aberg, C.; Dawson, K. A. Suppression of Nanoparticle Cytotoxicity Approaching *in Vivo* Serum Concentrations: Limitations of *in Vitro* Testing for Nanosafety. *Nanoscale* **2014**, *6*, 14180–14184.
52. Ge, C.; Du, J.; Zhao, L.; Wang, L.; Liu, Y.; Li, D.; Yang, Y.; Zhou, R.; Zhao, Y.; Chai, Z.; et al. Binding of Blood Proteins to Carbon Nanotubes Reduces Cytotoxicity. *Proc. Natl. Acad. Sci. U.S.A.* **2011**, *108*, 16968–16973.
53. Zhou, R.; Huang, X.; Margulis, C. J.; Berne, B. J. Hydrophobic Collapse in Multidomain Protein Folding. *Science* **2004**, *305*, 1605–1609.
54. Liu, P.; Huang, X.; Zhou, R.; Berne, B. J. Observation of a Dewetting Transition in the Collapse of the Melittin Tetramer. *Nature* **2005**, *437*, 159–162.
55. Lerf, A.; He, H.; Forster, M.; Klinowski, J. Structure of Graphite Oxide Revisited. *J. Phys. Chem. B* **1998**, *102*, 4477–4482.
56. Shih, C. J.; Lin, S.; Sharma, R.; Strano, M. S.; Blankschtein, D. Understanding the pH-Dependent Behavior of Graphene Oxide Aqueous Solutions: A Comparative Experimental and Molecular Dynamics Simulation Study. *Langmuir* **2012**, *28*, 235–241.
57. Medhekar, N. V.; Ramasubramaniam, A.; Ruoff, R. S.; Shenoy, V. B. Hydrogen Bond Networks in Graphene Oxide Composite Paper: Structure and Mechanical Properties. *ACS Nano* **2010**, *4*, 2300–2306.
58. Gómez-Navarro, C.; Meyer, J. C.; Sundaram, R. S.; Chuvilin, A.; Kurasch, S.; Burghard, M.; Kern, K.; Kaiser, U. Atomic Structure of Reduced Graphene Oxide. *Nano Lett.* **2010**, *10*, 1144–1148.
59. Ganguly, A.; Sharma, S.; Papakonstantinou, P.; Hamilton, J. Probing the Thermal Deoxygenation of Graphene Oxide Using High-Resolution *in Situ* X-Ray-Based Spectroscopies. *J. Phys. Chem. C* **2011**, *115*, 17009–17019.
60. O'Brien, E. P.; Stan, G.; Thirumalai, D.; Brooks, B. R. Factors Governing Helix Formation in Peptides Confined to Carbon Nanotubes. *Nano Lett.* **2008**, *8*, 3702–3708.
61. Liu, J.; Yang, Z.; Li, H.; Gu, Z.; Garate, J. A.; Zhou, R. Dewetting Transition Assisted Clearance of (NFGAILS) Amyloid Fibrils from Cell Membranes by Graphene. *J. Chem. Phys.* **2014**, *141*, 22D520.
62. Hua, L.; Huang, X.; Liu, P.; Zhou, R.; Berne, B. J. Nanoscale Dewetting Transition in Protein Complex Folding. *J. Phys. Chem. B* **2007**, *111*, 9069–9077.
63. Krone, M. G.; Hua, L.; Soto, P.; Zhou, R.; Berne, B. J.; Shea, J.-E. Role of Water in Mediating the Assembly of Alzheimer Amyloid-Beta Abeta16−22 Protofilaments. *J. Am. Chem. Soc.* **2008**, *130*, 11066–11072.
64. Zhou, R. Trp-Cage: Folding Free Energy Landscape in Explicit Water. *Proc. Natl. Acad. Sci. U.S.A.* **2003**, *100*, 13280–13285.
65. Jimenez-Cruz, C. A.; Kang, S.; Zhou, R. Large Scale Molecular Simulations of Nanotoxicity. *Wiley Interdiscip. Rev.: Syst. Biol. Med.* **2014**, *6*, 329–343.
66. Bernstein, F. C.; Koetzle, T. F.; Williams, G. J. B.; Meyer, E. F.; Brice, M. D.; Rodgers, J. R.; Kennard, O.; Shimanouchi, T.; Tasumi, M. The Protein Data Bank. *Eur. J. Biochem.* **1977**, *80*, 319–324.
67. Brown, J. H.; Volkmann, N.; Jun, G.; Henschen-Edman, A. H.; Cohen, C. The Crystal Structure of Modified Bovine Fibrinogen. *Proc. Natl. Acad. Sci. U.S.A.* **2000**, *97*, 85–90.

68. Brightbill, H. D.; Jeet, S.; Lin, Z.; Yan, D.; Zhou, M.; Tan, M.; Nguyen, A.; Yeh, S.; Delarosa, D.; Leong, S. R.; et al. Antibodies Specific for a Segment of Human Membrane IgE Deplete IgE-Producing B Cells in Humanized Mice. *J. Clin. Invest.* **2010**, *120*, 2218–2229.
69. Wally, J.; Halbrooks, P. J.; Vonrhein, C.; Rould, M. A.; Everse, S. J.; Mason, A. B.; Buchanan, S. K. The Crystal Structure of Iron-Free Human Serum Transferrin Provides Insight into Inter-Lobe Communication and Receptor Binding. *J. Biol. Chem.* **2006**, *281*, 24934–24944.
70. Guex, N.; Peitsch, M. C. SWISS-MODEL and the Swiss-PdbViewer: An Environment for Comparative Protein Modeling. *Electrophoresis* **1997**, *18*, 2714–2723.
71. MacKerell, A. D.; Bashford, D.; Bellott; Dunbrack, R. L.; Evanseck, J. D.; Field, M. J.; Fischer, S.; Gao, J.; Guo, H.; Ha, S.; et al. All-Atom Empirical Potential for Molecular Modeling and Dynamics Studies of Proteins. *J. Phys. Chem. B* **1998**, *102*, 3586–3616.
72. Humphrey, W.; Dalke, A.; Schulten, K. VMD: Visual Molecular Dynamics. *J. Mol. Graphics* **1996**, *14*, 33–38.
73. Jorgensen, W.; Chandrasekhar, J.; Madura, J.; Impey, R.; Klein, M. Comparison of Simple Potential Functions for Simulating Liquid Water. *J. Chem. Phys.* **1983**, *79*, 926–935.
74. Lindahl, E.; Hess, B.; van der Spoel, D. GROMACS 3.0: A Package for Molecular Simulation and Trajectory Analysis. *J. Mol. Model.* **2001**, *7*, 306–317.
75. Bussi, G.; Donadio, D.; Parrinello, M. Canonical Sampling through Velocity Rescaling. *J. Chem. Phys.* **2007**, *126*, 014101.
76. Parrinello, M.; Rahman, A. Polymorphic Transitions in Single-Crystals—A New Molecular-Dynamics Method. *J. Appl. Phys.* **1981**, *52*, 7182–7190.
77. Darden, T.; York, D.; Pedersen, L. Particle Mesh Ewald: An $N\cdot\log(N)$ Method for Ewald Sums in Large Systems. *J. Chem. Phys.* **1993**, *98*, 10089–10092.
78. Hess, B.; Bekker, H.; Berendsen, H. J. C.; Fraaije, J. G. E. M. LINCS: A Linear Constraint Solver for Molecular Simulations. *J. Comput. Chem.* **1997**, *18*, 1463–1472.
79. Miyamoto, S.; Kollman, P. A. SETTLE: An Analytical Version of the SHAKE and RATTLE Algorithm for Rigid Water Models. *J. Comput. Chem.* **1992**, *13*, 952–962.
80. Zuo, G.; Zhou, X.; Huang, Q.; Fang, H.; Zhou, R. Adsorption of Villin Headpiece onto Graphene, Carbon Nanotube, and C60: Effect of Contacting Surface Curvatures on Binding Affinity. *J. Phys. Chem. C* **2011**, *115*, 23323–23328.